(Title page)

Mechanical Performance of Laser Powder Bed Fused Ti-6Al-4V: The Influence of Filter Condition and Part Location

Mohammad Salman Yasin[1,2], Kevin Stonaker[3], Shuai Shao[1,2], Nima Shamsaei[1,2,*]

[1]*National Center for Additive Manufacturing Excellence (NCAME), Auburn University, Auburn, AL 36849, USA*

[2]*Department of Mechanical Engineering, Auburn University, Auburn, AL 36849, USA*

[3]*William J. Hughes Technical Center, Federal Aviation Administration (FAA), Atlantic City, NJ 08405, USA*

* Corresponding author: shamsaei@auburn.edu

Tel: (334) 844-4839

Submitted to:

Additive Manufacturing Letters

August 2024

Abstract

Deteriorated filter condition in laser powder bed fusion (L-PBF) systems may negatively impact shield gas flow, causing inadequate spatter particle/plume removal, leading to laser beam attenuation and reduction in melt pool depth, and potentially causing more frequent formation of volumetric defects. This work investigated the effects of filter condition and part location on the micro-/defect-structure and mechanical behavior, including tensile and fatigue, of Ti-6Al-4V parts fabricated by L-PBF. Interestingly, within the manufacturer recommended service intervals, no specific effect of filter condition could be observed on the micro-/defect-structure or the mechanical behavior of the fabricated parts. However, the parts' defect-structures were affected by their location, with ones located near the center of the build plate having less porosity than the ones located away. Although these defects did not affect the tensile properties, they frequently observed to initiate fatigue cracks (the critical defects sizes were often in the range of a few tens of micrometers). Therefore, their sensitivity to location resulted in the location dependence of the fatigue behavior.

Keywords: Additive manufacturing; Laser powder bed fusion (L-PBF/LB-PBF); Gas flow; Fatigue behavior; Part location

Nomenclature and abbreviations

ANOVA	Analysis of variance
BSE	Backscattered electron
√area	Size of crack initiating defects following Murakami's method
EBSD	Electron backscattered diffraction
EL	Elongation to failure
IPF	Inverse pole figure
L-PBF	Laser powder bed fusion/laser powder bed fused
OEM	Original equipment manufacturer
$\rho_{relative}$	Relative density
SEM	Scanning electron microscope/microscopy
Ti-64	Ti-6Al-4V
UTS	Ultimate tensile strength
XCT	X-ray computed tomography
YS	Yield strength

1 Introduction

Laser powder bed fusion (L-PBF), one of the most popular additive manufacturing processes, promise significantly higher design freedom than traditional manufacturing processes thanks to their near-net shaping capability, which makes it an attractive technology for many potential applications, such as those in aerospace, automotive, and healthcare sectors. L-PBF systems use laser to induce targeted melting within thin layers of powder (with thickness typically being in the range of 20-100 μm) successively to fabricate parts in a layer-by-layer manner [1,2]. However, during localized melting of the powder, gas-plumes consisting of by-products such as vaporized metal as well as ejected powder and spatter particles are formed. If these by-products are generated in excess or not removed properly, the laser beam may attenuate, leading to debits in energy delivered to the melt pool. This reduction in energy would result in inadequate overlap between layers or molten tracks and cause lack-of-fusion defects, which can be very detrimental to the fatigue behavior of the fabricated part [3–6]. To mitigate these issues, a continuous flow of shield gas is typically employed to sweep across the powder bed in a closed-loop system, effectively removing the by-products [7–9].

In many L-PBF systems, such as EOS M290 and Renishaw AM500Q, the shield gas initially enters the build chamber through multiple inlet nozzles and displaces the oxygen and other impurities through the exhaust. After achieving a sufficiently low oxygen level to establish an inert atmosphere, the external gas supply is either shut off or reduced to maintain a positive pressure and counteract possible leaks. A schematic of the shield gas flow system of EOS M290 is shown in **Figure 1**. During fabrication, different nozzles deliver the shield gas serving multiple purposes. The top inlet nozzle fulfils a dual function of safeguarding the laser window from contamination and promoting the removal of the soot and gas-plumes within the build chamber. The bottom inlet nozzle directs by-products from above the powder bed towards the extraction nozzle. The extracted gas then flows through the filter system before entering

the build chamber again [10]. A uniform flow of shield gas from the bottom inlet nozzle is critical in ensuring a minimal variation in defect content in the fabricated parts [11]. Non-uniformity in the shield gas flow can lead to localized laser beam scattering and attenuation, causing inconsistencies in melt pool depths, which may increase the population of volumetric defects [12,13].

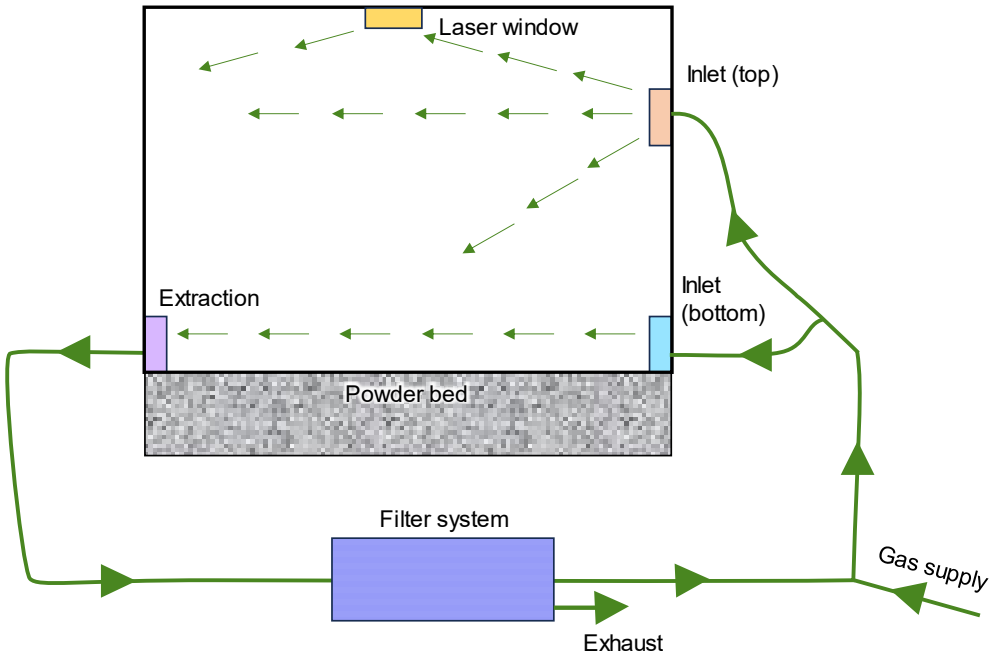

Figure 1: Schematic of the gas flow system in a typical L-PBF machine.

The uniformity of shield gas flow over the print bed depends on various factors such as gas type and flow rate, inlet and extraction nozzle design, and the filter system—to name a few. While the influence of some aspects of shield gas flow have been discussed in literature [14–16], the potential impact of the filter systems' condition on the shield gas flow and consequently the part quality, remains unclear. In addition, although the original equipment manufacturers (OEM) recommend periodic filter changes to ensure consistent shield gas flow, the understanding on how potential filter quality degradations within such intervals can affect printed part quality is still lacking in the literature.

Over time and with continued use, the filters may become clogged due to by-product deposition, and potentially obstruct the shield gas recirculation in the build chamber or cause backflow through the extraction nozzle. The resultant non-uniform shield gas flow across the powder bed can potentially increase the population and/or size of volumetric defects and adversely impact the mechanical behavior, especially fatigue [17,18]. Stress concentrations at the volumetric defects can lead to localized plastic deformation and accelerated fatigue crack initiation [8,19]. This potential effect of filter condition on defects and fatigue behavior is expected to be especially prominent in fine grained materials who exhibit great defect-sensitivity, such as Ti-6Al-4V (Ti-64). In the machined surface condition, fatigue failure of Ti-64 has been reported to always initiate from volumetric defects and its high cycle fatigue performance to be correlated with specific features of these defects, such as size, shape, and location [20–22].

Therefore, in this study, the effect of filter's condition on the micro-/defect-structure and mechanical behavior, including tensile and fatigue properties, of L-PBF Ti-64 is investigated. This investigation focuses on two filter conditions: before and after a scheduled end-of-life filter change. Furthermore, the effect of part location on the micro-/defect-structure and mechanical behavior has also been assessed. This manuscript is organized as the following: a brief overview of the experimental methodology is presented in Section 2; in Section 3, the experimental results are discussed; and finally, the conclusions of this work are drawn in Section 4.

2 Material and methods

In this study, a batch of plasma atomized Ti-64 powder supplied by AP&C (a Colibrium Additive company, Canada) was used for part fabrication. Prior to this study, the powder was used once and there was a sufficient powder to complete both builds in this project without further reuse. In its virgin state, the Ti-64 powder's nominal powder size distribution ranged from 15 to 45 μm. Prior to fabrication, the powder was sieved with a 63 μm mesh to ensure the removal of extremely large particles and agglomerates. Parts were produced vertically (see **Figures 2** (a) and (b) for fabrication layout) in an EOS M290 with OEM recommended process parameters. Some of the major process parameters included a laser power of 280 W, a laser speed of 1200 mm/s, a hatch distance of 140 μm, and a layer thickness of 30 μm.

Two identical builds were conducted with the filter condition as the only variable. One build was completed before the scheduled end-of-life filter change and the other one was completed immediately after installing the new filter system. For the first build, approximately 100 hours were left before the OEM recommended end-of-life filter change. The life of a new filter was 2500 hours. While EOS uses build time as an indicator of filter condition, in reality, the filter health can depend on factors such as the material, gas flow, and build plate density. Other OEMs such as Renishaw and 3D systems use pressure drop (i.e., more pressure drop indicates more clogging and therefore poorer filter health). EOS M290 also monitors the pressure drop of filters, but it does not trigger a replacement warning if the value stays below a threshold. The results obtained in this study are specific to the current use case and machine. In the following sections, builds, parts, microstructural samples, X-ray computed tomography (XCT) coupons, and specimens for the two conditions are designated with the prefix '*before*' and '*after*' in italic type face. Moreover, to examine the potential effect of part location on volumetric defect's content as well as their impact on mechanical properties all parts were divided into three regions of north, central, and south with respect to the direction of gas flow.

The north region was the closest to the inlet nozzle. A schematic illustration of the grouping is shown in **Figure 2** (b). Furthermore, the XCT coupons positioned across the build plate (i.e., NW, N, NE, W, C, E, SW, S, and SE) are labeled in **Figure 2** (b). The geometry of the XCT coupons are shown in **Figure 2** (f)

To ensure that the oxygen concentration in the build chamber did not influence the results of this study, the recorded data from EOS's in-built oxygen sensors for both builds were reviewed. The oxygen concentration in the build chamber at different layer heights for both builds are shown in **Figure 2** (c). Although slight variations in oxygen concentration could be seen between the two builds, it was consistently below the OEM recommended threshold of 1000 parts per million.

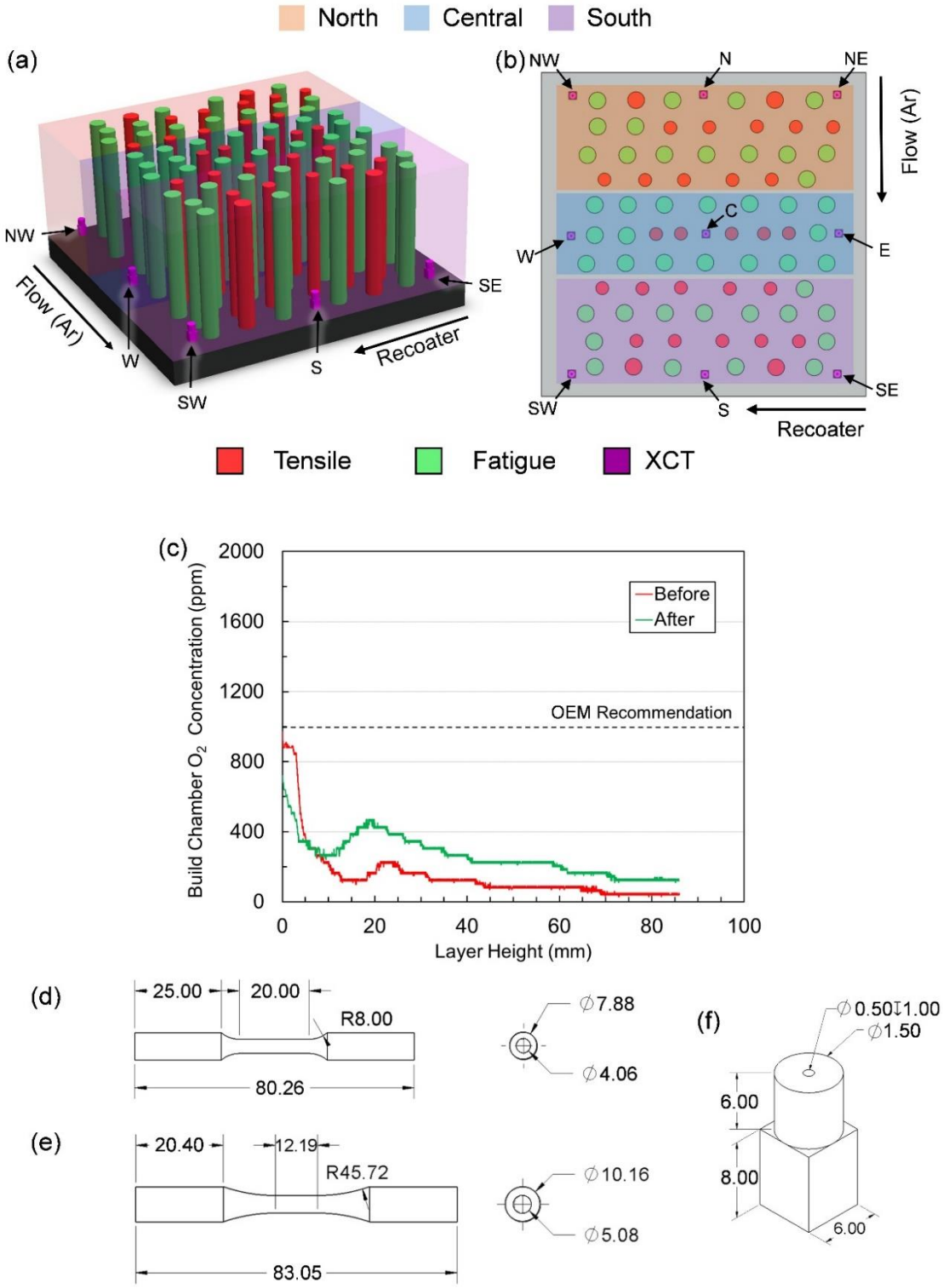

Figure 2: (a) and (b) Schematic of the fabrication layout used in isometric and top views. Parts in shaded boxes of orange, blue, and purple indicate north, central, and south regions of the build plate. (c) Oxygen concentration in the build chamber as a function of layer height for *before* and *after* builds. The black dash line indicates the OEM recommended threshold of build chamber oxygen concentration. (d) and (e) Geometries of tensile and fatigue specimens following ASTM E8M and E466. (f) Geometry of XCT coupon (all dimensions are in mm).

After fabrication, the XCT coupons and specimens were detached from the build plate, and the cylindrical parts were stress relieved at 704 °C for one hour in argon environment. The parts were then furnace cooled to room temperature. Microstructural samples were prepared by sectioning the grip-end of a fatigue specimen along the radial plane (i.e., the cross-section perpendicular to the building direction) from both builds and mounting in cold set resin. The mounts were ground using sandpapers ranging from 320 to 4000 grits and finally polished with 0.02 µm colloidal silica. Microstructural analysis was then conducted on the radial plane using a Zeiss Crossbeam 550 Scanning Electron Microscope (SEM) equipped with electron backscattered diffraction (EBSD) and backscattered electron (BSE) detectors. Some of the acquisition parameters used during EBSD analysis included a voltage of 20 kV, a current of 1500 pA, and a step size of 0.9 µm.

Seventeen XCT coupons were scanned to analyze the effect of filter condition and part location on the volumetric defect content using a ZEISS Xradia 620 Versa machine with a voxel size of 5 µm, a scan voltage of 140 kV, and a source power of 21 W. Note that one XCT coupon in the southwest location was not successfully fabricated due to support failure during the *before* build and could not be included for the analysis. This failure, which was due to a weakened support structure that caused the coupon's detachment when the recoater hit, appeared to be an isolated event and did not affect the rest of the build. The XCT data was reconstructed using Xradia Versa proprietary software and then post-processed using Fiji ImageJ and MATLAB. Furthermore, the equivalent sphere diameter was used in this study to measure the size of defects. Defects smaller than 20 µm (i.e., 4 voxels) were excluded from the analysis to reduce the risk of false-defect detection from noise.

From both builds, thirty-one cylindrical parts were machined to eleven tensile and twenty fatigue specimens, whose geometries had been specified in ASTM E8M [23] and E466 [24]. The schematics of the designs are shown in **Figures 2** (d) and (e). Tensile tests were

conducted at room temperature in displacement-controlled mode using a nominal strain rate of 0.06 mm/mm/min using an MTS landmark servo-hydraulic axial test frame equipped with a 100 kN load cell, and tests were continued until specimen rupture. Moreover, fully reversed force-controlled fatigue tests were conducted using the same machine for four different stress amplitudes, with a minimum of five specimens tested per stress amplitude per filter condition. Each fatigue test continued until the specimen ruptured. After testing, fractography was conducted using the SEM.

3 Results and Discussion

3.1 Micro-/defect-structure

The microstructure of both the *before* and *after* samples on the cross-section perpendicular to the build direction is shown in **Figure 3** using BSE micrographs and inverse pole figures (IPF) maps. The BSE micrographs indicate the presence of lamellar α and β phases, whose morphology does not significantly differ between the *before* and *after* conditions. The β phase appears in the BSE images (**Figures 3** (a) and (b)) as small, elongated, discrete features with bright contrast. Due to their small size, the EBSD scans could not effectively detect the β phase regions and only revealed a β fraction of < 1 %. For this reason, the β phase is not shown in the IPF maps in **Figures 3** (c) and (d). The IPF maps further confirms the lamellar morphology of the α phase and the similarity in the microstructure between the *before* and *after* conditions. The similarity in microstructure despite the filter change might indicate the efficient plume removal by the gas flow, leading to similar laser exposure and cooling rates of the specimens during the fabrication.

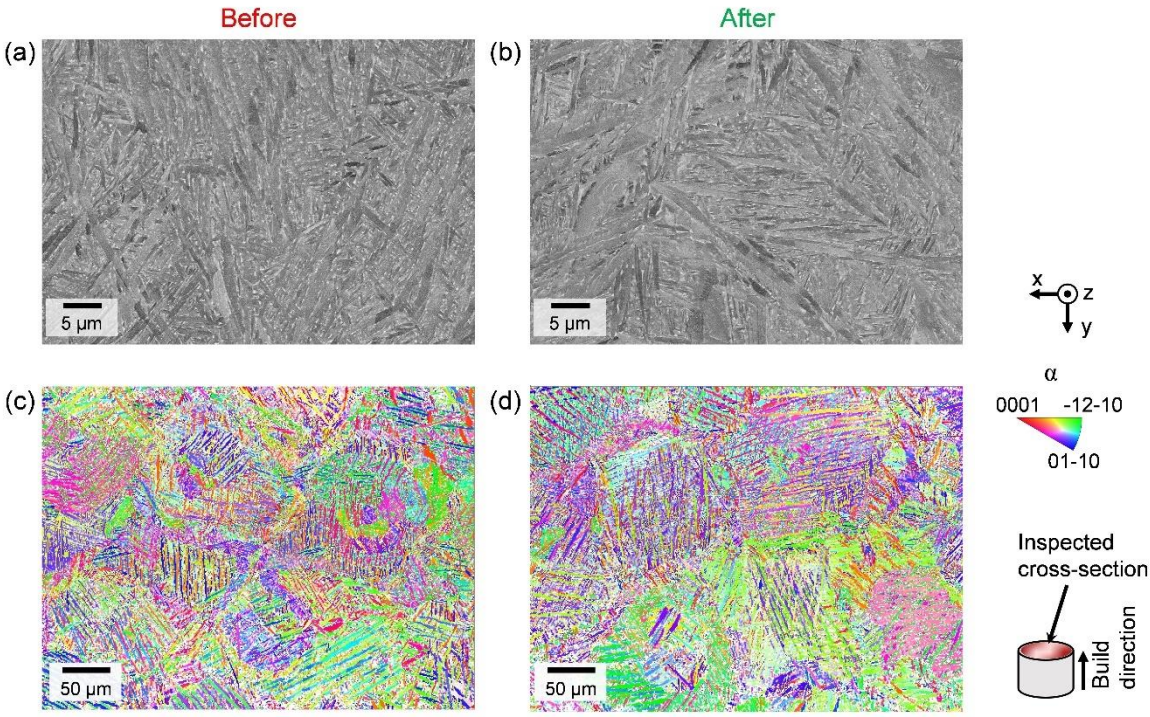

Figure 3: BSE micrographs and IPF maps on the cross-section perpendicular to the build direction: (a) and (c) for *before* specimens and (b) and (d) for *after* specimens. The IPF maps indicate the crystallographic directions along the inspected surface normal.

The spatial defect distribution in two XCT coupons, i.e., one *before* and one *after*, from the center of the build plate can be seen in **Figure 4** (a). Note that the markers used in **Figure 4** (a) indicate the defects' location and size but not the defects' shape. No significant clustering of defects was observed within the scanned volume, suggesting the defects to be randomly distributed. Additionally, the *before* and *after* XCT coupons exhibited similar relative densities ($\rho_{relative}$), with values of 99.9999 % and 99.9999 %, respectively. In both cases, no defects larger than 50 µm could be seen. Based on **Figure 4** (a), the filter condition apparently did not influence defect formation in the center of the build plate.

The XCT coupons' defect size distribution for each part location is summarized in the three-dimensional histograms shown in **Figures 4** (b) and (c) for the *before* and *after* conditions. The label on top of each column indicates $\rho_{relative}$ of the specific XCT coupon in that location. Note that the *before* XCT coupon in the southwest location could not be used for

the comparison (marked by x in **Figure 4** (b)) since it was not successfully fabricated. Among all the XCT coupons, the C coupon for both builds exhibited the least defects, as well as the highest $\rho_{relative}$, compared to the coupons elsewhere. This could be due to OEMs primarily ensuring the focus of the laser at the center of the build plate during calibration and the largest laser incidence angles occurring at the center of the build plate (see **Figure 5** (a)) [25,26]. Although F-Theta lenses have been widely used in L-PBF machines, including EOS M290, to minimize the difference in the incidence angle among different locations, such variation still persists, especially towards the periphery of the build plate (see **Figure 5** (b)). This can lead to elongation of laser spots, reducing laser energy density, shallower melt pools, and increased defect formation in the periphery [27–30]. Furthermore, comparing the coupons in the north region (i.e., NE, N, and NW) with the south region (i.e., SE, S, and SW) shown in **Figures 4** (b) and (c), no significant trends in either $\rho_{relative}$ or defect size distributions can be observed, indicating negligible overall dependence on the gas flow direction.

An analysis of **Figures 4** (b) and (c) also shows more defects for XCT coupons located in the east and west compared to their center counterparts. This trend was especially clear in the middle region of both the *before* and *after* builds. For instance, the count per volume for E, C, and W coupons of the *before* build were 4232, 73, and 4427 cm^{-3}, respectively. Similar observation could also be made for the *after* build. Interestingly, such a significant difference in defect populations was not reflected in the overall $\rho_{relative}$ of the coupons. For instance, in the middle region of the *before* build, the $\rho_{relative}$ difference between C and E coupons was 0.011 %, and between C and W coupons was 0.007 %.

Aside from the contributions from the laser incidence angle effect in the off-center locations, this might be due to powder segregation during recoating. Due to the dynamic particle-recoater interaction, powder particles tend to segregate during recoating, leading to the deposition of finer powder particles closer to the powder reservoir and coarser particles further

away [31–34]. Nevertheless, powder segregation can depend on numerous factors such as the particle size and shape distribution, recoater type and geometry, gap between the powder bed and recoater, and surface characteristics of solidified parts, to name a few [35–37]. Moreover, fine particles are more prone to agglomeration and formation of large powder clusters due to the higher surface-to-volume ratio and interparticle friction [38,39]. Such powder clusters can disturb the powder bed by creating empty spaces between the particles [40]. This disruption, coupled with the agglomerates' lower energy absorption, increased the likelihood of lack-of-fusion defect formation in the regions near the powder reservoir [41–43]. Similarly, the locations away from the powder reservoir were also prone to induce lack-of-fusion defects because of the prevalence of coarse particles and the associated poor melting due to their larger inter-particle spacing and lower energy absorption efficiency [44,45]. Indeed, the presence of these lack-of-fusion defects, typically irregularly shaped and exhibiting low roundness (defined as the ratio of the equivalent sphere diameter to the maximum axis of the fitted ellipse), in the east and west regions was confirmed in the XCT scan results [46,47]. Specifically, **Figures 4** (d) and (e) show the roundness values for *before* and *after* coupons, where the coupons located in east and west region of the build plate appear to contain more irregular defects than the ones in the center of the build plate. For instance, except for the exceptions in the south region of the *before* build due to the missing SW coupon, the occurrence of the lowest defect roundness was always in the east and west regions.

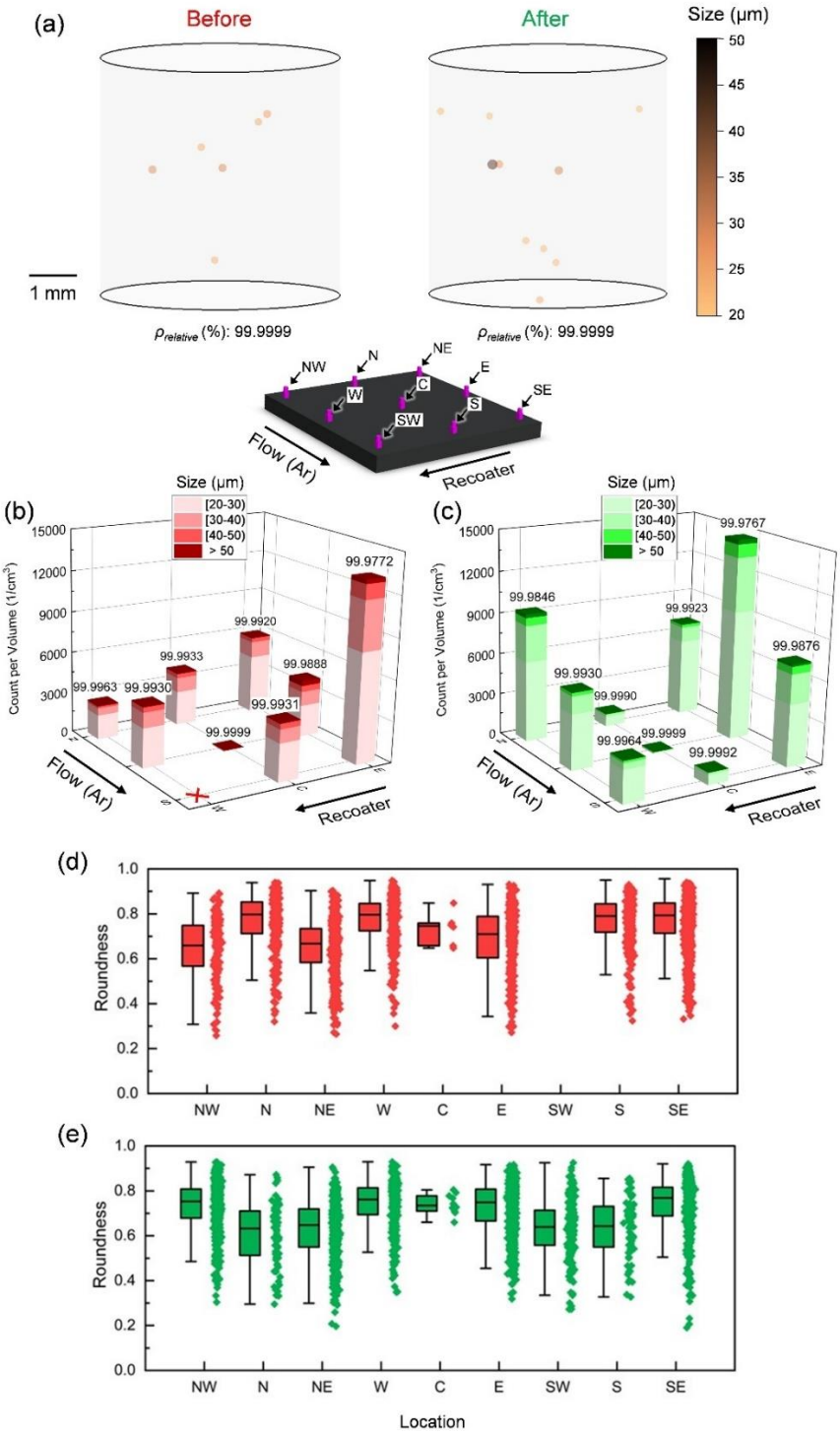

Figure 4: (a) Three-dimensional visualization of volumetric defects' size and spatial distribution of XCT coupons located at the center of the build plate from *before* and *after* builds. The color bar indicates the size of defects. (b) and (c) The distribution of defect sizes, extracted from gage section of XCT coupons, for *before* and *after* builds, respectively. The label above each column shows the $\rho_{relative}$ value for that specific location. (d) and (e) Boxplots with all datapoints next to it for each location showing the distribution of defects' roundness for *before* and *after* builds, respectively.

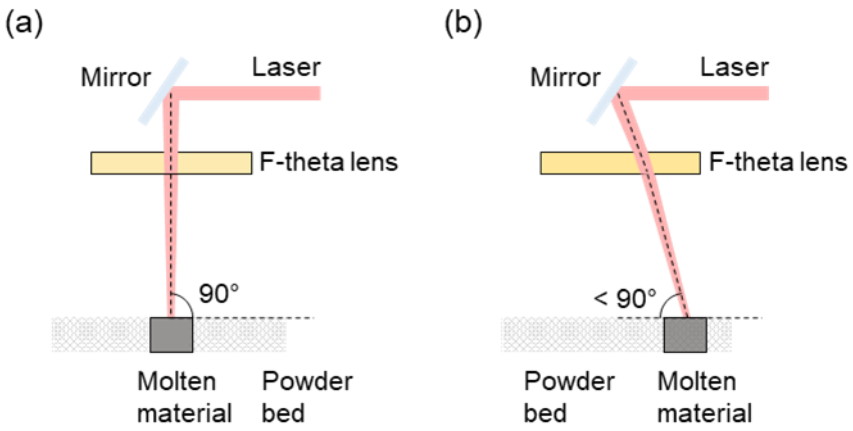

Figure 5: Schematic showing the laser incidence angle for parts fabricated in the (a) center and (b) off-center location on the build plate.

3.2 Tensile behavior

The tensile properties, namely, ultimate tensile strength (UTS), yield stress (YS), and elongation to failure (EL), of L-PBF Ti-64 of the *before* and *after* specimens are shown in **Figure 6** (a), indicating no effect of filter change on the tensile properties. The figure also shows the minimum strength (UTS of 895 MPa and YS of 825 MPa) and ductility (EL of 10 %) requirements outlined in ASTM F2924-14 for vertically fabricated L-PBF Ti-64 specimens [48]. Regardless of the filter condition, the minimum requirements of strength and ductility were satisfied in this study. Furthermore, the tensile properties showed minimal variation among the 11 tested specimens from different locations in both conditions (standard deviations of 6.8 MPa, 8.5 MPa, and 1.5 % in the *before* condition, and 7.5 MPa, 15.7 MPa, and 2.9 % in the *after* condition for UTS, YS, and EL, respectively).

Despite the variation in defect content across locations (see **Figure 4**), the tensile properties showed minimal variation (see **Figure 6** (b)). This suggested that the presence of volumetric defects might not have affected the tensile behavior. This observation was consistent with the report of Refs. [8,49] that the tensile properties of highly dense additively manufactured materials ($\rho_{relative}$ > 99 %) did not depend on $\rho_{relative}$. Interestingly, **Figure 6** (b)

shows a very slight variation in tensile properties, especially in strength, which appears to be a function of part location and potentially the result of the difference in laser incidence angle in the off-center locations. As the laser incidence angle decreases in the off-center locations, the laser spot size increases and the laser energy density decreases. The resulting changes in cooling rates may have caused slight changes in the microstructure and, thus, tensile properties [27,50]. Nevertheless, the differences in the tensile properties across different locations were very small.

Additionally, analysis of variance (ANOVA) was used to statistically verify the effect of filter condition and part location on the tensile properties. During the ANOVA analysis, specimens were pre-classified as *before* and *after* for filter condition and as north, central, and south for part location. The p-values for YS, UTS, and EL considering for filter condition and part location are listed in **Table 1.** All but one p-value was greater than 0.05, suggesting that the filter condition and part location did not significantly impact the tensile properties.

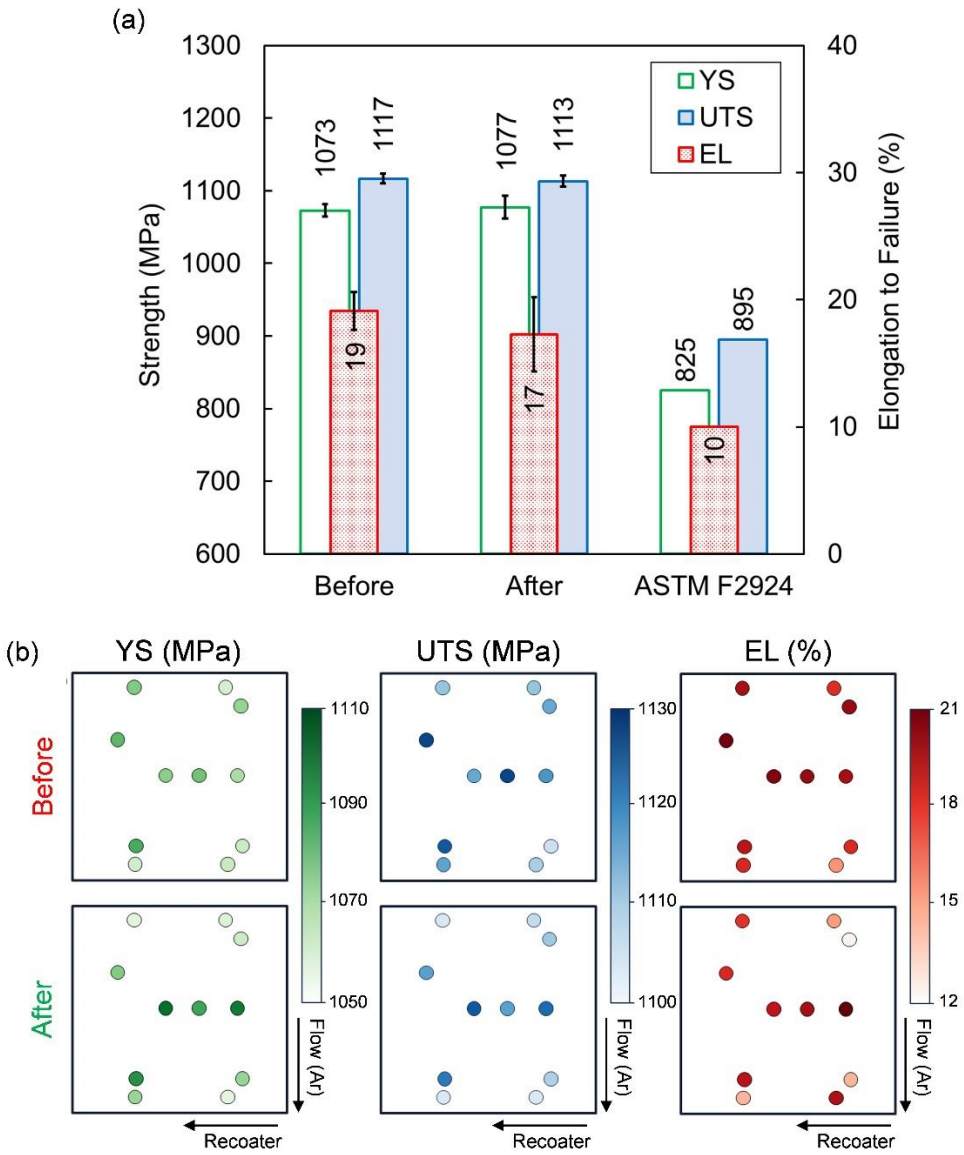

Figure 6: Comparison of tensile properties for (a) specimens of *before* and *after* conditions, and (b) specimens fabricated at different locations on the build plate.

Table 1: p-values for ANOVA analysis of the tensile property.

	Tensile property		
Variable	YS	UTS	EL
Filter condition	0.39	0.21	0.08
Part location	0.04	0.06	0.07

The fracture surfaces of tensile specimens for both filter conditions are shown in **Figure 7**. The fractography images, in both cases, revealed a typical cup-and-cone feature, which was

indicative of ductile fracture behavior. Moreover, the fracture surfaces could be divided into two main regions: an interior region with irregular and fibrous appearance and a peripheral region of shear lips. At higher magnifications, shallow dimples could be seen in the interior region for both conditions.

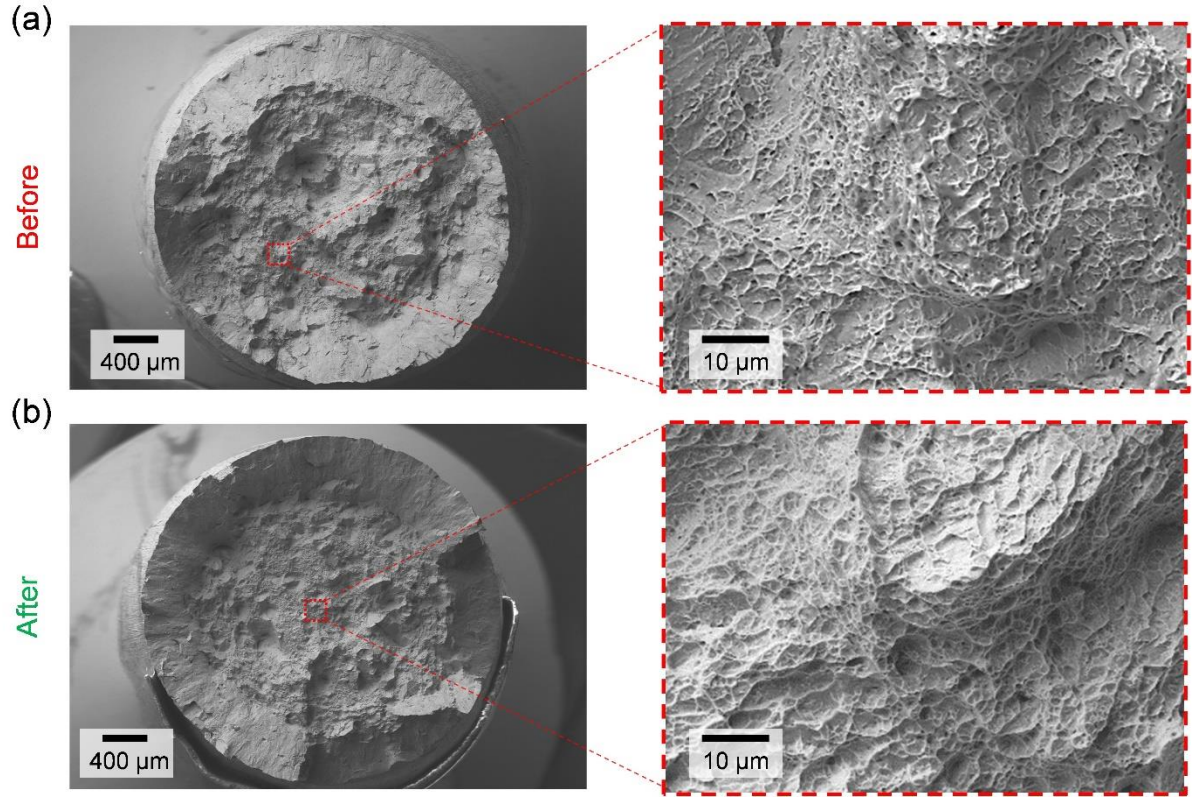

Figure 7: Fractography of tensile specimens for (a) *before* and (b) *after* conditions.

3.3 Fatigue behavior

The results of fully reversed axial fatigue tests are shown in **Figures 8** (a) and (b) isolating the effect of filter condition and part location, respectively. Note that two specimens did not fail from the gage and the tests could not be continued due to grip break-off. These specimens are marked using inclined arrows in **Figures 8** (a) and (b). Some scatter in the fatigue lives at different stress amplitudes can be seen in the figures, in particular for the specimens tested at 500 and 400 MPa. However, no clear correlation between the fatigue behavior and the filter condition could be observed. On the other hand, considering the effect of part locations on fatigue behavior (see **Figure 8** (b)), the central specimens can be seen to

generally perform better than the north and south specimens. Moreover, for the specimens tested in this study, crack initiation primarily occurred due to either surface or near-surface lack-of-fusion defects. Two such crack initiating defects are shown in **Figures 8** (c) and (d), where the outlines of the defect shapes are traced in red.

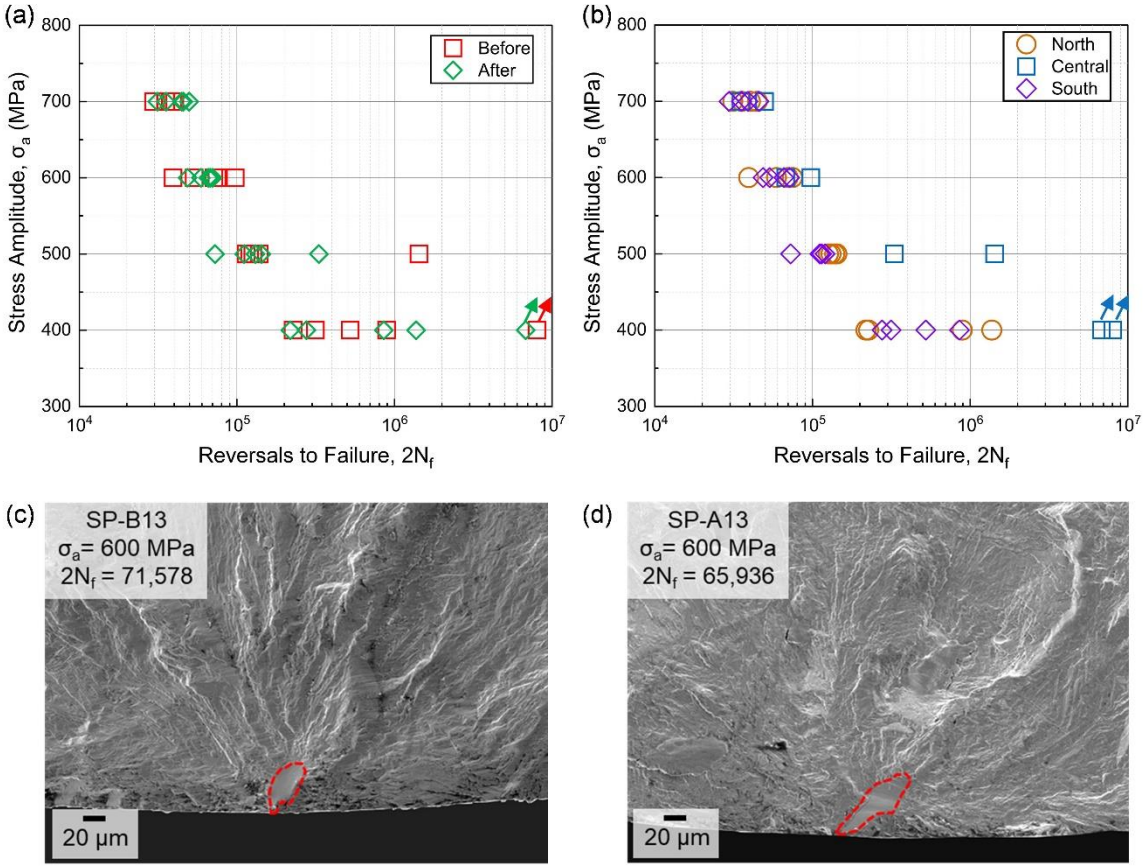

Figure 8: (a) and (b) Fatigue behavior of L-PBF Ti-64 specimens plotted highlighting the effects of filter condition and part location, respectively. The inclined arrows indicate the specimens which experienced grip failure. (c) and (d) Fatigue fracture surfaces of *before* and *after* specimens, respectively, showing the critical defect in red outline.

The stress-life data is replotted for *before* and *after* specimens in **Figures 9** (a) and (b), with marker size and color representing the crack initiating defects' size (√area). √area was measured following Murakami's approach [51–53] and based on the convex hull of the defect's two-dimensional projection on the loading plane. Furthermore, in **Figures 9** (c) and (d), the

markers are reorganized based on their respective part location for both builds. **Figures 9** (a) and (b) show that the critical defect size is similar for both filter conditions, indicating negligible effect of filter condition on the fatigue behavior of L-PBF Ti-64.

In addition, larger √area generally corresponded to shorter fatigue lives except for a few anomalies. For instance, two *before* specimens tested at 500 MPa stress amplitude exhibited fatigue lives of 126,228 and 1,429,308 reversals, with √area values of 58 and 21 μm. On the other hand, another *before* specimen, tested at the same stress amplitude, showed a shorter fatigue life of 114, 312 reversals with smaller √area value of 48 μm. Such an exception in fatigue lives might have originated from the shape of the critical defects along with the size [21,54]. In order to better quantify the effect of part location on the critical defect size, the normal distributions of √area for north, central and south regions are shown in **Figure 9** (e), combining data from both builds. This shows the √area generally increases for specimens located farther from the center of the build plate. The XCT analysis (see **Figure 4** (b)) strongly supports this observation, revealing similar trends of increased quantity and size of defects for coupons away from the center. These observations further imply that part location had significant effect on the fatigue behavior of L-PBF Ti-64.

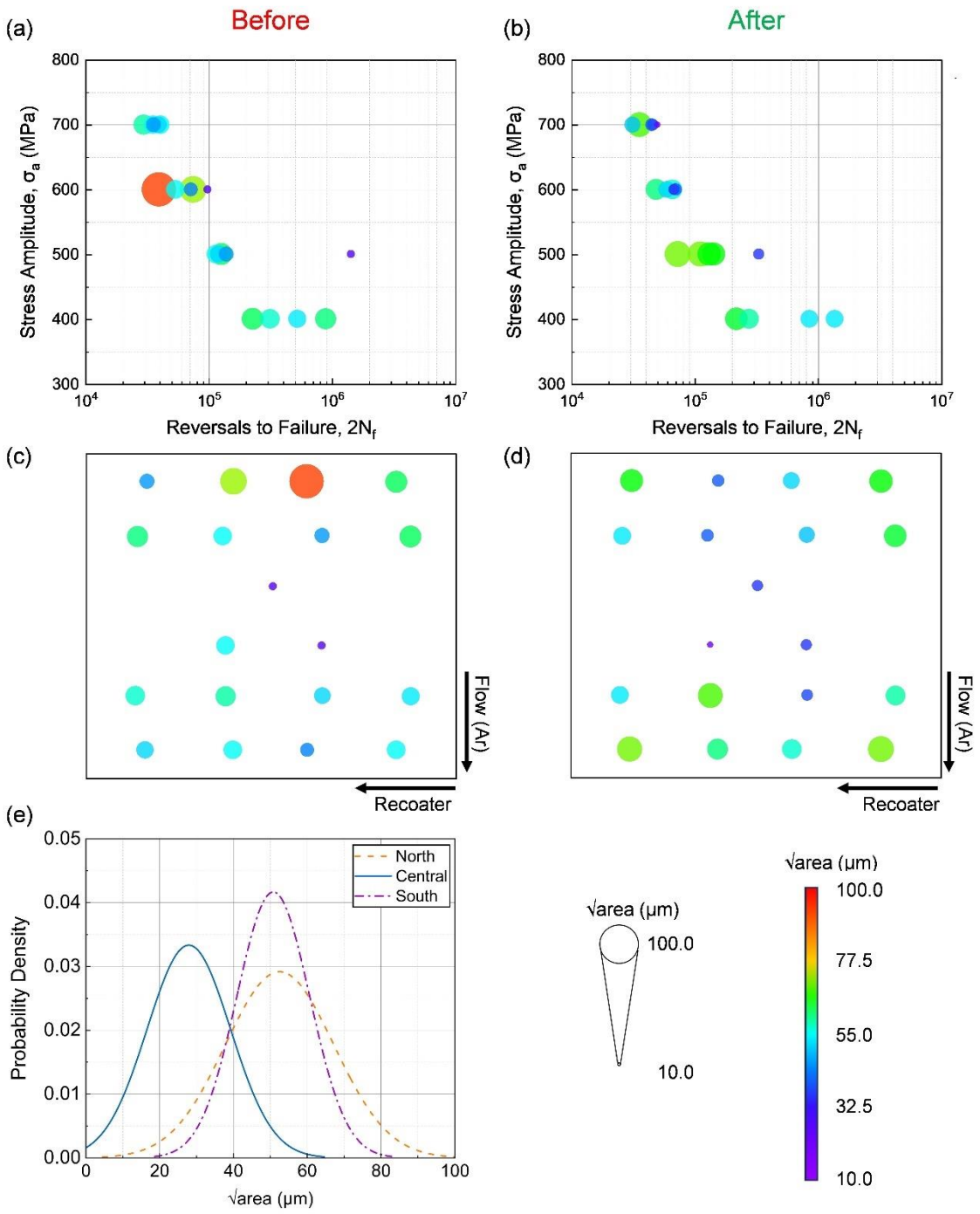

Figure 9: (a) and (b) Stress-life behavior of L-PBF Ti-64 along with their √area. (c) and (d) √area for each specimen plotted according to their part location on the build plate. The marker size and color indicates the √area (the scales are shown in the bottom right side of the figure). (e) the normal distributions of √area for fatigue specimens in the north, central and south regions.

4 Conclusions

This study aimed to understand the effects of filter condition and part location on the micro-/defect-structure and mechanical behavior, including both tensile and fatigue, of L-PBF Ti-64. Overall, neither the micro-/defect-structure nor mechanical properties were affected by the filter's condition, as long as the filter is replaced based on the guideline provided by the OEM. However, part location played an important role in the defect-structure of L-PBF Ti-64; the coupons located in the center of the build plate were found to contain fewer defects than those further away. While part location did not significantly impact the tensile properties, it affected the fatigue behavior. Specimens located in the central region of the build plate exhibited longer fatigue lives. This difference in fatigue behavior was due to their differences in the defect-structure. While the results of this study were generated based on Ti-64 fabricated by EOS M290, the conclusions drawn should at least be qualitatively applicable to other L-PBF machines.

Declaration of competing interest

The authors declare that they have no known competing financial interests or personal relationships that could have appeared to influence the work reported in this paper.

Acknowledgments

This work was partially supported by the Federal Aviation Administration [grant number FAA-12-C-AM-AU-003]; and the National Science Foundation (NSF) [grant number 2319690].

References

[1] S. Chowdhury, N. Yadaiah, C. Prakash, S. Ramakrishna, S. Dixit, L.R. Gupta, D. Buddhi, Laser powder bed fusion: a state-of-the-art review of the technology, materials, properties & defects, and numerical modelling, Journal of Materials Research and Technology. 20 (2022) 2109–2172. https://doi.org/10.1016/j.jmrt.2022.07.121.

[2] L. Bian, N. Shamsaei, J. Usher, Laser-based additive manufacturing of metal parts: modeling, optimization, and control of mechanical properties, CRC Press, 2017.

[3] A. Ladewig, G. Schlick, M. Fisser, V. Schulze, U. Glatzel, Influence of the shielding gas flow on the removal of process by-products in the selective laser melting process, Additive Manufacturing. 10 (2016) 1–9. https://doi.org/10.1016/j.addma.2016.01.004.

[4] H. Shen, P. Rometsch, X. Wu, A. Huang, Influence of Gas Flow Speed on Laser Plume Attenuation and Powder Bed Particle Pickup in Laser Powder Bed Fusion, JOM. 72 (2020) 1039–1051. https://doi.org/10.1007/s11837-020-04020-y.

[5] A. Soltani-Tehrani, M.S. Yasin, S. Shao, N. Shamsaei, Effects of Stripe Width on the Porosity and Mechanical Performance of Additively Manufactured Ti-6Al-4V Parts, in: 2021 International Solid Freeform Fabrication Symposium, University of Texas at Austin, 2021. https://hdl.handle.net/2152/90708.

[6] A. Yadollahi, N. Shamsaei, Additive manufacturing of fatigue resistant materials: Challenges and opportunities, International Journal of Fatigue. 98 (2017) 14–31. https://doi.org/10.1016/j.ijfatigue.2017.01.001.

[7] C. Pauzon, E. Hryha, P. Forêt, L. Nyborg, Effect of argon and nitrogen atmospheres on the properties of stainless steel 316 L parts produced by laser-powder bed fusion, Materials & Design. 179 (2019) 107873. https://doi.org/10.1016/j.matdes.2019.107873.

[8] A. Mostafaei, C. Zhao, Y. He, S.R. Ghiaasiaan, B. Shi, S. Shao, N. Shamsaei, Z. Wu, N. Kouraytem, T. Sun, J. Pauza, J. V. Gordon, B. Webler, N.D. Parab, M. Asherloo, Q. Guo, L. Chen, A.D. Rollett, Defects and anomalies in powder bed fusion metal additive manufacturing, Current Opinion in Solid State and Materials Science. 26 (2022) 100974. https://doi.org/10.1016/j.cossms.2021.100974.

[9] P.Y. Shcheglov, S.A. Uspenskiy, A.V. Gumenyuk, V.N. Petrovskiy, M. Rethmeier, V.M. Yermachenko, Plume attenuation of laser radiation during high power fiber laser welding, Laser Physics Letters. 8 (2011) 475–480. https://doi.org/10.1002/lapl.201110010.

[10] B. Peikang, Z. Zhanyong, B. Liu, Y. Xibin, J. Wang, D. Jingzhi, SLM forming device for multiple metal powder materials, US 10,661,382, 2020.

[11] B. Ferrar, L. Mullen, E. Jones, R. Stamp, C.J. Sutcliffe, Gas flow effects on selective laser melting (SLM) manufacturing performance, Journal of Materials Processing Technology. 212 (2012) 355–364. https://doi.org/10.1016/j.jmatprotec.2011.09.020.

[12] C. Tenbrock, T. Kelliger, N. Praetzsch, M. Ronge, L. Jauer, J.H. Schleifenbaum, Effect of laser-plume interaction on part quality in multi-scanner Laser Powder Bed Fusion, Additive Manufacturing. 38 (2021) 101810. https://doi.org/10.1016/j.addma.2020.101810.

[13] D.C. Deisenroth, J. Neira, J. Weaver, H. Yeung, Effects of shield gas flow on meltpool variability and signature in scanned laser melting, in: International Manufacturing Science and Engineering Conference, American Society of Mechanical Engineers, 2020: p. V001T01A017.

[14] G. Zhang, J. Li, J. Li, X. Zhou, A. Wang, 3D metal printer dust filter structural optimal design and key performance research, Materials & Design. 183 (2019) 108114. https://doi.org/10.1016/j.matdes.2019.108114.

[15] J.S. Weaver, A. Schlenoff, D.C. Deisenroth, S.P. Moylan, Inert gas flow speed measurements in laser powder bed fusion additive manufacturing, 2021.

https://doi.org/10.6028/NIST.AMS.100-43.

[16] C.N.G. Pauzon, Tailored process gases for laser powder bed fusion, Chalmers Tekniska Hogskola (Sweden), 2021.

[17] N. Shamsaei, A. Yadollahi, L. Bian, S.M. Thompson, An overview of Direct Laser Deposition for additive manufacturing; Part II: Mechanical behavior, process parameter optimization and control, Additive Manufacturing. 8 (2015) 12–35. https://doi.org/10.1016/j.addma.2015.07.002.

[18] H.D. Nguyen, A. Pramanik, A.K. Basak, Y. Dong, C. Prakash, S. Debnath, S. Shankar, I.S. Jawahir, S. Dixit, D. Buddhi, A critical review on additive manufacturing of Ti-6Al-4V alloy: microstructure and mechanical properties, Journal of Materials Research and Technology. 18 (2022) 4641–4661. https://doi.org/10.1016/j.jmrt.2022.04.055.

[19] S. Wang, J. Ning, L. Zhu, Z. Yang, W. Yan, Y. Dun, P. Xue, P. Xu, S. Bose, A. Bandyopadhyay, Role of porosity defects in metal 3D printing: Formation mechanisms, impacts on properties and mitigation strategies, Materials Today. 59 (2022) 133–160. https://doi.org/10.1016/j.mattod.2022.08.014.

[20] M.S. Dodaran, M. Muhammad, N. Shamsaei, S. Shao, Synergistic effect of microstructure and defects on the initiation of fatigue cracks in additively manufactured Inconel 718, International Journal of Fatigue. 162 (2022) 107002. https://doi.org/10.1016/j.ijfatigue.2022.107002.

[21] S. Shao, A. Poudel, N. Shamsaei, A linear elastic finite element approach to fatigue life estimation for defect laden materials, Engineering Fracture Mechanics. 285 (2023) 109298. https://doi.org/10.1016/j.engfracmech.2023.109298.

[22] K.D. Rekedal, D. Liu, Investigation of the high-cycle fatigue life of selective laser melted and hot isostatically pressed Ti-6Al-4V, in: Additive Manufacturing Handbook, CRC Press, 2017: pp. 569–574.

[23] ASTM International, ASTM E8 / E8M-21, Standard Test Methods for Tension Testing of Metallic Materials, West Conshohocken, PA, 2021.

[24] ASTM International, ASTM E466-15, Standard practice for conducting force controlled constant amplitude axial fatigue tests of metallic materials, West Conshohocken, PA, 2015.

[25] J. Berez, E. Dushaj, E. Jost, C. Saldaña, K. Fu, Measurement of focal plane error in laser powder bed fusion machines, Additive Manufacturing Letters. 9 (2024) 100196. https://doi.org/10.1016/j.addlet.2024.100196.

[26] P.E. Verboven, Distortion correction formulas for pre-objective dual galvanometer laser scanning, Applied Optics. 27 (1988) 4172. https://doi.org/10.1364/AO.27.004172.

[27] P. Fathi-Hafshejani, A. Soltani-Tehrani, N. Shamsaei, M. Mahjouri-Samani, Laser incidence angle influence on energy density variations, surface roughness, and porosity of additively manufactured parts, Additive Manufacturing. 50 (2022) 102572. https://doi.org/10.1016/j.addma.2021.102572.

[28] E. Li, H. Shen, L. Wang, G. Wang, Z. Zhou, Laser shape variation influence on melt pool dynamics and solidification microstructure in laser powder bed fusion, Additive Manufacturing Letters. 6 (2023) 100141. https://doi.org/https://doi.org/10.1016/j.addlet.2023.100141.

[29] S. Rott, A. Ladewig, K. Friedberger, J. Casper, M. Full, J.H. Schleifenbaum, Surface roughness in laser powder bed fusion – Interdependency of surface orientation and laser incidence, Additive Manufacturing. 36 (2020) 101437. https://doi.org/10.1016/j.addma.2020.101437.

[30] T.P. Le, X. Wang, K.P. Davidson, J.E. Fronda, M. Seita, Experimental analysis of powder layer quality as a function of feedstock and recoating strategies, Additive Manufacturing. 39 (2021) 101890. https://doi.org/10.1016/j.addma.2021.101890.

[31] Y. Lee, S. Simunovic, A. Gurnon, Quantification of Powder Spreading Process for Metal Additive Manufacturing, Oak Ridge National Lab.(ORNL), Oak Ridge, TN (United States), Oak Ridge, TN (United States), 2019. https://doi.org/10.2172/1615799.

[32] U. Ali, Y. Mahmoodkhani, S. Imani Shahabad, R. Esmaeilizadeh, F. Liravi, E. Sheydaeian, K.Y. Huang, E. Marzbanrad, M. Vlasea, E. Toyserkani, On the measurement of relative powder-bed compaction density in powder-bed additive manufacturing processes, Materials & Design. 155 (2018) 495–501. https://doi.org/10.1016/j.matdes.2018.06.030.

[33] A. Soltani-Tehrani, M. Habibnejad-Korayem, S. Shao, M. Haghshenas, N. Shamsaei, Ti-6Al-4V powder characteristics in laser powder bed fusion: The effect on tensile and fatigue behavior, Additive Manufacturing. 51 (2022) 102584. https://doi.org/10.1016/j.addma.2021.102584.

[34] D. Yao, J. Wang, M. Li, T. Zhao, Y. Cai, X. An, R. Zou, H. Zhang, H. Fu, X. Yang, Q. Zou, Segregation of 316L stainless steel powder during spreading in selective laser melting based additive manufacturing, Powder Technology. 397 (2022) 117096. https://doi.org/10.1016/j.powtec.2021.117096.

[35] M. Stephan, G. Roux, A. Burr, C. Ablitzer, J.-P. Garandet, Identification of the influential DEM contact law parameters on powder bed quality and flow in additive manufacturing configurations, Powder Technology. 429 (2023) 118937. https://doi.org/10.1016/j.powtec.2023.118937.

[36] A. Mussatto, R. Groarke, A. O'Neill, M.A. Obeidi, Y. Delaure, D. Brabazon, Influences of powder morphology and spreading parameters on the powder bed topography uniformity in powder bed fusion metal additive manufacturing, Additive Manufacturing. 38 (2021) 101807. https://doi.org/10.1016/j.addma.2020.101807.

[37] G. Miao, W. Du, Z. Pei, C. Ma, A literature review on powder spreading in additive manufacturing, Additive Manufacturing. 58 (2022) 103029. https://doi.org/10.1016/j.addma.2022.103029.

[38] M.A. Balbaa, A. Ghasemi, E. Fereiduni, M.A. Elbestawi, S.D. Jadhav, J.-P. Kruth, Role of powder particle size on laser powder bed fusion processability of AlSi10mg alloy, Additive Manufacturing. 37 (2021) 101630. https://doi.org/10.1016/j.addma.2020.101630.

[39] J. Muñiz-Lerma, A. Nommeots-Nomm, K. Waters, M. Brochu, A Comprehensive Approach to Powder Feedstock Characterization for Powder Bed Fusion Additive Manufacturing: A Case Study on AlSi7Mg, Materials. 11 (2018) 2386. https://doi.org/10.3390/ma11122386.

[40] G. Jacob, C.U. Brown, A. Donmez, The influence of spreading metal powders with different particle size distributions on the powder bed density in laser-based powder bed

fusion processes, US Department of Commerce, National Institute of Standards and Technology, 2018.

[41] J.H. Tan, W.L.E. Wong, K.W. Dalgarno, An overview of powder granulometry on feedstock and part performance in the selective laser melting process, Additive Manufacturing. 18 (2017) 228–255. https://doi.org/10.1016/j.addma.2017.10.011.

[42] F. Chu, K. Zhang, H. Shen, M. Liu, W. Huang, X. Zhang, E. Liang, Z. Zhou, L. Lei, J. Hou, A. Huang, Influence of satellite and agglomeration of powder on the processability of AlSi10Mg powder in Laser Powder Bed Fusion, Journal of Materials Research and Technology. 11 (2021) 2059–2073. https://doi.org/10.1016/j.jmrt.2021.02.015.

[43] A. Phua, P.S. Cook, C.H.J. Davies, G.W. Delaney, Powder spreading over realistic laser melted surfaces in metal additive manufacturing, Additive Manufacturing Letters. 3 (2022) 100039. https://doi.org/10.1016/j.addlet.2022.100039.

[44] L.E.T. Mathias, V.E. Pinotti, B.F. Batistão, N. Rojas-Arias, G. Figueira, A.F. Andreoli, P. Gargarella, Metal powder as feedstock for laser-based additive manufacturing: From production to powder modification, Journal of Materials Research. 39 (2024) 19–47. https://doi.org/10.1557/s43578-023-01271-8.

[45] J. Tang, R. Wróbel, P. Scheel, W. Gaechter, C. Leinenbach, E. Hosseini, The role of process parameters and printing position on meltpool variations in LPBF Hastelloy X: Insights into laser-plume interaction, Additive Manufacturing Letters. 9 (2024) 100203. https://doi.org/10.1016/j.addlet.2024.100203.

[46] A. Poudel, M.S. Yasin, J. Ye, J. Liu, A. Vinel, S. Shao, N. Shamsaei, Feature-based volumetric defect classification in metal additive manufacturing, Nature Communications. 13 (2022) 6369. https://doi.org/10.1038/s41467-022-34122-x.

[47] R. Snell, S. Tammas-Williams, L. Chechik, A. Lyle, E. Hernández-Nava, C. Boig, G. Panoutsos, I. Todd, Methods for Rapid Pore Classification in Metal Additive Manufacturing, JOM. 72 (2020) 101–109. https://doi.org/10.1007/s11837-019-03761-9.

[48] ASTM International, ASTM F2924-14, Standard Specification for Additive Manufacturing Titanium-6 Aluminum-4 Vanadium with Powder Bed Fusion, West Conshohocken, PA, 2014.

[49] H. Gong, K. Rafi, H. Gu, G.D. Janaki Ram, T. Starr, B. Stucker, Influence of defects on mechanical properties of Ti–6Al–4V components produced by selective laser melting and electron beam melting, Materials & Design. 86 (2015) 545–554. https://doi.org/10.1016/j.matdes.2015.07.147.

[50] A. Ebrahimi, M. Sattari, A. Babu, A. Sood, G.-W.R.B.E. Römer, M.J.M. Hermans, Revealing the effects of laser beam shaping on melt pool behaviour in conduction-mode laser melting, Journal of Materials Research and Technology. 27 (2023) 3955–3967. https://doi.org/10.1016/j.jmrt.2023.11.046.

[51] Y. Murakami, Metal Fatigue, Elsevier, 2002. https://doi.org/10.1016/B978-0-08-044064-4.X5000-2.

[52] U. Zerbst, M. Madia, C. Klinger, D. Bettge, Y. Murakami, Defects as a root cause of fatigue failure of metallic components. I: Basic aspects, Engineering Failure Analysis. 97 (2019) 777–792. https://doi.org/10.1016/j.engfailanal.2019.01.055.

[53] Y. Murakami, S. Beretta, Small defects and inhomogeneities in fatigue strength: experiments, models and statistical implications, Extremes. 2 (1999) 123–147. https://doi.org/10.1023/A:1009976418553.

[54] N. Sanaei, A. Fatemi, N. Phan, Defect characteristics and analysis of their variability in metal L-PBF additive manufacturing, Materials & Design. 182 (2019) 108091. https://doi.org/10.1016/j.matdes.2019.108091.